JOURNAL OF COMPUTATIONAL PHYSICS 6, 430–448 (1970)

A Numerical Model for Toroidal Plasma Containment with Flow*

NIELS K. WINSOR, JOHN L. JOHNSON,† AND JOHN M. DAWSON

Plasma Physics Laboratory, Princeton University, Princeton, New Jersey 08540

Received March 17, 1970

A numerical model has been developed to study the confinement of low-pressure plasmas in simple axially symmetric configurations. The equations contain the effects of resistivity, plasma inertia, and pressure gradients along the field. The model is applied to a simple magnetic geometry that includes the effects of curvature, rotational transform, and shear. An explicit difference scheme is derived for the numerical solution with this prescribed geometry. Results of calculations with the model are compared to a similarity solution for resistive diffusion in a cylinder, and to calculations of quasistationary diffusion in a torus. Finally, the onset of plasma rotation is demonstrated and its development to a steady-state rotation is observed.

1. INTRODUCTION

The determination of the properties of a plasma confined in a toroidal magnetic field is complicated by the nonlinear behavior of the governing equations, by the number and complexity of the physical phenomena involved, and by the geometry. Thus, most analytic treatments have many weakening assumptions and approximations and leave much to be desired. Here we describe a computer program for studying such confinement that utilizes a fluid description and should fill in some of the gaps. It contains many of the features of a real plasma and, at the same time, is sufficiently simple to obtain results without excessive use of machine time.

The simplest plasma model begins with the ideal hydromagnetic equations and the assumption that the configuration is static—there is no mass flow. Kruskal and Kulsrud [1] found a variational principle and proposed a thought experiment to demonstrate the existence of equilibrium solutions for configurations where the magnetic field lines form nested toroidal surfaces. They identified the constraints that must be specified to characterize the system. One must prescribe the shape

* This work was performed under the auspices of the U. S. Atomic Energy Commission, Contract AT(30-1)-1238; also, use was made of computer facilities supported in part by National Science Foundation Grant NSF-GP579.

† On loan from Westinghouse Research Laboratories.

of some bounding magnetic surface (or, equivalently, the currents in external conductors), the pressure on each magnetic surface, and the rotational transform (or, equivalently, the net current) on each surface. Explicit evaluation of such configurations has been done, both for axially symmetric systems [2] and for stellarators using expansion techniques [3, 4]. Analytical efforts to obtain equilibrium solutions for a more realistic model [5–7] have indicated the way in which nonideal terms restrict the class of acceptable solutions, but have not shed much light on the nature of steady-state configurations. Recent work has shown that the static case is unstable [8], and that a rotating equilibrium is established in the presence of additional dissipation processes such as viscosity [9].

A numerical approach, alternative to the one presented here, is to follow the behavior of a collection of guiding-center particles in a prescribed magnetic field [10–12]. These calculations employ Poisson's equation to determine the electric field from the difference between the electron and ion charge densities. For such calculations the mesh spacing must be comparable to the Debye length, which is many orders of magnitude smaller than the dimensions of a reasonable plasma containment device. Thus a very large number of grid points is required. Furthermore, the time step in such a calculation must be shorter than the plasma period and thus is many orders of magnitude smaller than the characteristic times of acoustic motion, hydromagnetic instabilities, and resistive diffusion—the phenomena of interest in containment studies. These requirements make realistic simulations using particle models prohibitively expensive in computer time.

For these reasons we have developed a simulation model utilizing fairly simple fluid equations. The major motivation has been to understand toroidal configurations where mass flow and other nonideal effects are important. Therefore, we have incorporated plasma inertia, pressure gradients along the magnetic field, and electrical resistivity into the initial model. We have restricted consideration to static magnetic fields, an assumption that greatly simplifies the problem and is realistic for the low-pressure devices currently being studied, in which field annihilation [13] is not important. We follow the development of the system in real time. This fluid model is described in the next section and a finite-difference approximation to it is developed in Section 3. The numerical stability criteria for these explicit difference equations are described in Appendix II.

The major results obtained to date are as follows:

While developing the program we found electrostatic oscillations, with a period equal to that required for a sound wave to propagate around the torus divided by $(1 + \iota^2/8\pi^2)^{1/2}$, reminiscent of the Pfirsch–Schlüter factor [14]. This was first thought to be a numerical instability. However, analysis of the equations for small z-independent perturbations about a static solution leads to a dispersion relation that is in good agreement with the numerical observations. This work is reported elsewhere [15].

If the configuration is nearly static, the usual predictions [16] of classical diffusion can be recovered. For large resistivity, however, plasma inertia associated primarily with flow along the magnetic field lines must be balanced by pressure gradients in the magnetic surfaces. The modification of diffusion due to this effect is discussed in Section 4.

If the plasma is given a small initial rotation velocity, this flow increases exponentially in agreement with recent theoretical predictions [8, 17, 18]. The numerical results are described in Section 5.

2. Model

We use the scalar-pressure fluid model [19] described by the following equations (in Gaussian units):

$$\rho\left(\frac{\partial \mathbf{v}}{\partial t} + \mathbf{v}\cdot\nabla\mathbf{v}\right) = \frac{1}{c}\mathbf{J}\times\mathbf{B} - \nabla(p_e + p_i), \tag{1}$$

$$\mathbf{E} + \frac{1}{c}\mathbf{v}\times\mathbf{B} = \eta\mathbf{J}, \tag{2}$$

$$\frac{\partial\rho}{\partial t} + \nabla\cdot\rho\mathbf{v} = 0, \tag{3}$$

$$p_i = p_e = \frac{\rho kT}{m} = \frac{1}{2}\rho v_{\text{th}}^2, \tag{4}$$

$$\frac{1}{c}\frac{\partial\mathbf{B}}{\partial t} = -\nabla\times\mathbf{E}, \tag{5}$$

$$\frac{4\pi}{c}\mathbf{J} = \nabla\times\mathbf{B}, \tag{6}$$

$$\nabla\cdot\mathbf{B} = 0. \tag{7}$$

Here we have assumed that the ions and electrons have the same constant temperature. Current interest in low-pressure systems motivates separation of magnetic field into two parts: $\mathbf{B} = \mathbf{B}_{\text{external}} + \mathbf{B}_{\text{plasma}}$, with $\mathbf{B}_{\text{external}}$ a prescribed static field and $\mathbf{B}_{\text{plasma}}$ sufficiently small that it can be neglected. Thus the field is magnetostatic: $\partial\mathbf{B}/\partial t = 0$; consequently, Eq. (5) reduces to the electrostatic condition

$$\mathbf{E} = -\nabla\phi, \tag{8}$$

and Eq. (6) is replaced by the charge neutrality condition

$$\nabla\cdot\mathbf{J} = 0. \tag{9}$$

The terms on the right side of Eq. (1) must be nearly equal; otherwise balance would be restored by a rapid relaxation with characteristic time $\eta c^2/v_{\text{Alfvén}}^2$, as

can be seen for the case of cylindrical geometry. Therefore, straightforward integration of these equations fails unless very short time steps and a high-order difference scheme are used. A method of solution other than direct time integration is needed.

Knorr [5] studied the equilibrium problem for systems of this type; Karlson [6] and Viswanathan [7] corrected and extended his results. Following the lines of their analytic methods, we have developed a prescription for calculating the plasma motion. The procedure, illustrated in Fig. 1, is the following:

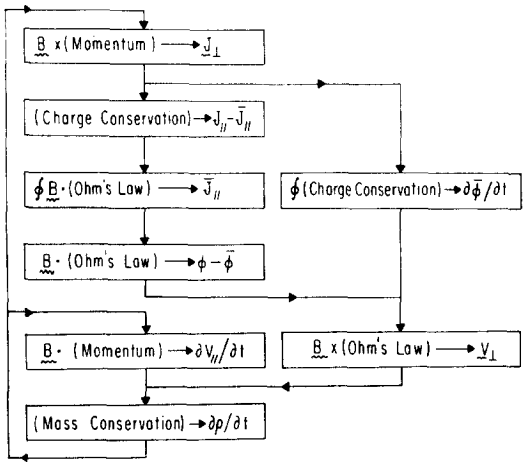

FIG. 1. Computational procedure.

Use the component of Eq. (1) parallel to **B** to advance $v_\parallel$ in time, and the other two components to compute $\mathbf{J}_\perp$ at each time step. In the numerical program this introduces a small error, in that the current value of $\partial \mathbf{v}_\perp/\partial t$ is not known and must be approximated by its value as derived in the previous time step. This is justified both physically and numerically. In the low-pressure limit, only $\mathbf{E} \times \mathbf{B}$ drifts and resistive diffusion serve to transport mass across the magnetic field; perpendicular inertia would be important only if it could couple with magnetic field motion to produce Alfvén waves. The error introduced by this approximation is smaller in magnitude than the truncation error in the ∇p term. The numerical aspects of this approximation are discussed near the end of Appendix I.

Rewrite Eq. (9),

$$\mathbf{B} \cdot \nabla(\mathbf{J} \cdot \mathbf{B}/B^2) = -\nabla \cdot \mathbf{J}_\perp , \tag{10}$$

and integrate along a magnetic field line to obtain $J_\parallel$, up to an arbitrary surface

function (i.e., a function which is constant on each magnetic surface). Similarly, integrate the parallel component of Eq. (2),

$$\mathbf{B} \cdot \nabla\phi = -\eta \mathbf{J} \cdot \mathbf{B}, \tag{11}$$

to determine ϕ to within a surface function. Use the other two components of Eq. (2) to determine $\mathbf{v}_\perp$, and then use Eq. (3) to advance ρ in time.

The solvability condition [1] for Eq. (11),

$$\int \mathbf{J} \cdot \mathbf{B}\, dS / |\nabla\Psi| = 0 \tag{12}$$

(where dS is the element of surface area and Ψ is a surface label), determines the constant of integration (surface function) for Eq. (10). Similarly, substitution of Eq. (1) for $\mathbf{J}_\perp$ and then Eq. (2) for $\mathbf{v}_\perp$ into the solvability condition for Eq. (10) yields a partial differential equation (in Ψ and t) to advance the surface function $\bar{\phi}$ of Eq. (11) in time. After integration with respect to Ψ and application of the divergence theorem, this condition (no charge accumulation on a magnetic surface) can be written

$$\int \mathbf{J} \cdot \nabla\Psi\, dS / |\nabla\Psi| = 0. \tag{13}$$

This completes the system of equations for advancing the plasma in time.

Initial and boundary conditions must also be specified; they depend on the difference scheme as well as the mathematical form of the equations. The quantities that are integrated forward in time are the parallel velocity $v_\parallel$, the density ρ, and the radial gradient of the average electrostatic potential $d\bar{\phi}/dr$. These are the basic variables of the problem, and clearly must be assigned initial values.

In the solution scheme outlined here, the partial time derivative of the perpendicular velocity is small. Equations (1), (2), (10), and (13) determine the perpendicular velocity in terms of the basic variables, through equations that do not involve time derivatives if $\partial\mathbf{v}_\perp/\partial t$ is neglected. In the program we iterate these equations to obtain initial values of the velocity that are consistent with the basic variables. This is most easily accomplished if the initial velocities are small. A natural choice of preinitialization variables is therefore $\rho = \rho(r)$, $v_\parallel = 0$, $\partial\bar{\phi}/\partial r = 0$.

Boundary conditions are also required at the wall for all time. For calculations with this model, it is satisfactory to take the density at the wall constant and small compared to interior values. Then $v_\parallel$ and $\partial\bar{\phi}/\partial r$ can be computed at the wall in the same way that they are computed on the remainder of the mesh. Tests have shown that the results of calculations are insensitive to changes in density at the wall, provided the density remains small.

For some extensions of the model, e.g., including the Hall-effect terms in Ohm's law, the results are sensitive to the boundary conditions. Such difficulties can be circumvented by inserting a region of constant low density and vanishing velocity between the boundary and the active plasma region. Radial transport in this region is slow compared to resistive diffusion times in the body of the plasma, so the insulation associated with this outer region will persist during the course of a run.

We are using the idealized magnetic field model described by Knorr [5]. Our coordinate system (r, θ, z) has a metric given by

$$ds^2 = dr^2 + r^2\, d\theta^2 + [1 - (r/R)\cos\theta]^2\, dz^2, \tag{14}$$

and is shown in Fig. 2. It reduces to a cylindrical coordinate system (along the minor axis of the torus) when the major radius R is made infinite. The magnetic field is

$$\mathbf{B} = \mathbf{B}_0[\mathbf{e}_\theta f(r) + \mathbf{e}_z]/[1 - (r/R)\cos\theta]. \tag{15}$$

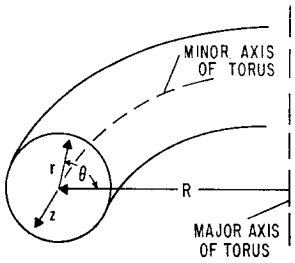

FIG. 2. The toroidal coordinate system.

It satisfies Eq. (7) and corresponds to a toroidal field plus a field due to a purely axial current

$$\mathbf{J}_0 = \frac{c}{4\pi}\,\mathbf{e}_z B_0\,\frac{1}{r}\,\frac{\partial}{\partial r}\,\frac{rf(r)}{1 - (r/R)\cos\theta}\,. \tag{16}$$

With this field the magnetic surfaces are concentric tori. The function $f(r)$ is related to the rotational transform by

$$f(r) = r\iota(r)/2\pi(R^2 - r^2)^{1/2}. \tag{17}$$

We think of this transform as really being imposed by external helical windings in a stellarator, or by internal currents not carried by the plasma (such as those of a hard core in a levitron). For a stellarator, the current of Eq. (16) is fictitious but this model reproduces many of the features of the actual system.

This choice for the magnetic field permits some important simplifications in the numerical model. For example, in the (r, θ, z) coordinate system, the acceleration terms are

$$\mathbf{v} \cdot \nabla \mathbf{v} = \mathbf{e}_r \mathbf{v} \cdot \nabla v_r + \mathbf{e}_\theta \mathbf{v} \cdot \nabla v_\theta + \mathbf{e}_z \mathbf{v} \cdot \nabla v_z + \boldsymbol{\Omega} \times \mathbf{v}, \tag{18}$$

where

$$\boldsymbol{\Omega} = \frac{v_\theta}{r} \mathbf{e}_z + \frac{v_z(\mathbf{e}_r \sin \theta + \mathbf{e}_\theta \cos \theta)}{R - r \cos \theta}. \tag{19}$$

Here $\boldsymbol{\Omega}$ has a simple physical interpretation: It represents the coordinate rotation, per unit time, following a fluid element. To see this, consider an infinitesimal displacement $r\, d\theta = v_\theta\, dt$ in the $\mathbf{e}_\theta$ direction. Then the coordinate system rotates through an angle $d\Omega = v_\theta / r$ about the axis $\mathbf{e}_z$. The relatively simple form of Eq. (19) is due to our particular choice of the coordinate system.

Since the coordinate surfaces and magnetic surfaces coincide, the magnetic line integrals for $J_\parallel$ and ϕ and the solvability conditions, Eqs. (12) and (13), take simple forms in the difference equations. It is necessary to satisfy these integrals accurately, since their solutions, $J_\parallel$ and ϕ, play a dominant role in determining the dynamics of the motion.

3. Difference Equations

The continuous fluid is approximated by equal-area cells on a cylindrical mesh, with density and velocity calculated on alternate points [20]. The boundaries of these cells are equally spaced rays of constant θ, and circles equally spaced in r^2. The components of velocity are displaced one half step in their respective directions, relative to the density. In addition, the velocities are displaced one half step in time. This allows proper centering of the differences.

The continuity equation is evaluated using centered differences in space and time [21]; it is used to advance the density in time. In terms of the divergence operator,

$$(\nabla \cdot \mathbf{u})^t_{r,\theta} = \frac{r_{r+1/2} N_{r+1/2,\theta} u^t_{r+1/2,\theta} - r_{r-1/2} N_{r-1/2,\theta} u^t_{r-1/2,\theta}}{r_r N_{r,\theta}\, \delta r} + \frac{N_{r,\theta+1/2} u^t_{r,\theta+1/2} - N_{r,\theta-1/2} u^t_{r,\theta-1/2}}{r_r N_{r,\theta}\, \delta\theta}, \tag{20}$$

where δr measures the radial spacing of the mesh and

$$N = 1 - \frac{r}{R} \cos \theta. \tag{21}$$

The partial time derivative of the density is obtained from

$$\left(\frac{\delta\rho}{\delta t}\right)_{r,\theta}^{t+1/2} = -(\nabla \cdot \rho_f \mathbf{v})_{r,\theta}^{t+1/2}. \tag{22}$$

The quantity ρ_f is used to center the right side in time and is calculated similarly. Thus, density is advanced in time by

$$\rho_{r,\theta}^{t+1} = \rho_{r,\theta}^{t} + \delta t \left(\frac{\delta\rho}{\delta t}\right)_{r,\theta}^{t+1/2} \tag{23}$$

and

$$(\rho_f)_{r,\theta}^{t+3/2} = \rho_{r,\theta}^{t+1} + \frac{1}{2}\,\delta t \left(\frac{\delta\rho}{\delta t}\right)_{r,\theta}^{t+1/2}. \tag{24}$$

Space centering of Eq. (22) is accomplished by spatial averaging of ρ_f from adjacent mesh points.

The parallel component of the momentum equation is a convective differential equation for the parallel velocity,

$$\rho\left(\frac{\partial v_\parallel}{\partial t} + \mathbf{v} \cdot \nabla v_\parallel + \mathbf{e}_\parallel \cdot \boldsymbol{\Omega} \times \mathbf{v}\right) = -\mathbf{e}_\parallel \cdot \frac{2kT}{m} \nabla\rho. \tag{25}$$

This is integrated by the method of Courant, Isaacson, and Rees [22]. First we obtain the dimensionless vector

$$\mathbf{u} = \frac{\delta t}{\delta r} v_r \mathbf{e}_r + \frac{\delta t}{r\,\delta\theta} v_\theta \mathbf{e}_\theta . \tag{26}$$

Then the backward space difference along $\mathbf{u}$ is used to advance $v_\parallel$. This can be written

$$\begin{aligned}(v_\parallel)_{r,\theta}^{t+1/2} = (1 - |u|)(v_\parallel)_{r,\theta}^{t-1/2} + |u_r|\,(v_\parallel)_{r-S_r,\theta}^{t-1/2} + |u_\theta|\,(v_\parallel)_{r,\theta-S_\theta}^{t-1/2} \\ - \delta t \left[\frac{2kT}{m} \nabla \ln\rho + \boldsymbol{\Omega} \times \mathbf{v}\right] \cdot \mathbf{e}_\parallel ,\end{aligned} \tag{27}$$

where $S_r = \operatorname{sgn}(u_r)$ and $S_\theta = \operatorname{sgn}(u_\theta)$.

In our geometry, Eq. (13) becomes

$$\oint \mathbf{e}_r \cdot \frac{\mathbf{B}}{B^2} \times \left[\frac{2kT}{m} \nabla\rho + \rho\left(\frac{\partial \mathbf{v}}{\partial t} + \mathbf{v} \cdot \nabla\mathbf{v}\right)\right] \frac{d\theta}{B} = 0. \tag{28}$$

This equation implicitly determines the surface function $\bar{\phi}$ (constant of integration) in the electrostatic potential. It can be rewritten as a convective partial differential

equation that explicitly advances $\bar{\phi}$ in time; this is done in Appendix II. We approximated $d\mathbf{v}_\perp/dt$ by its value from the previous time when advancing $v_\parallel$; we use the same approximation here. Thus Eq. (28) is rewritten

$$\oint \mathbf{e}_r \cdot \frac{\mathbf{B}}{B^2} \times \left\{ \frac{2kT}{m} \nabla\rho + \rho \left(\frac{\partial \mathbf{v}}{\partial t} + \mathbf{v} \cdot \nabla \mathbf{v} \right)^{t-1} + \rho \mathbf{e}_r \times \frac{\mathbf{B}}{B^2} \left[\left(\frac{\partial^2 \bar{\phi}}{\partial r\, \partial t} \right)^t - \left(\frac{\partial^2 \bar{\phi}}{\partial r\, \partial t} \right)^{t-1} \right] \right\} \frac{d\theta}{B} = 0, \tag{29}$$

where $\bar{\phi}$ is the surface function in the potential. Since $\bar{\phi}$ is independent of θ, the quantity $(\partial^2\bar{\phi}/\partial r\, \partial t)^t$ can be taken outside the integration, and Eq. (29) explicitly determines it. The time integral of this quantity then determines E_r and ϕ. The magnitude of the error introduced by the approximate treatment of $d\mathbf{v}_\perp/dt$ is small. However this approximation dictates the precise form of Eq. (29) because of numerical stability considerations.

The remaining calculations, J, $\mathbf{v}_\perp$, and the part of ϕ that varies on a surface, do not involve time integrals; they are explicit, and are easily centered in space and time. To achieve this centering, we let J_r occupy the same mesh points as v_θ , let J_θ and J_z occupy the v_r mesh points, and let $\phi - \bar{\phi}$ be displaced one half mesh spacing relative to ρ in r, θ, and t.

Two transport processes are present in this model: resistive diffusion and acoustic motion. Since the numerical difference techniques described above are explicit, each transport process introduces a numerical stability criterion. For all cases of physical interest, the stability requirement for sound is the more stringent one. (The calculation of this criterion is given in Appendix I.) It limits the step size to a few microseconds for typical stellarator parameters.

4. Diffusion

One obvious application of this simulation model is to investigate the effects of plasma inertia on classical diffusion in a torus.

If the inertial terms in Eq. (1) are negligibly small, plasma diffuses through a magnetic surface in this configuration at the rate [1, 16]

$$\begin{aligned} \int v_D \, dS &= \eta c^2 \int \frac{|\nabla p|^2}{B^2} \left(1 + \frac{J_\parallel{}^2}{J_\perp{}^2} \right) \frac{dS}{|\nabla p|} \\ &= \frac{(2\pi)^2 \eta c^2 p'(r)\, rR(1 + 3r^2/2R^2)}{B_0{}^2[1 + r^2\iota^2/(2\pi)^2 (R^2 - r^2)]} \\ &\quad \cdot \left\{ 1 + \frac{(2\pi)^2 (R^2 - r^2)}{r^2\iota^2} \left[1 - \frac{(1 - r^2/R^2)}{(1 + 3r^2/2R^2)} \right] \right\} \\ &\approx \frac{(2\pi)^2 \eta c^2 p'(r)\, rR[1 + 8\pi^2/\iota^2]}{B_0{}^2[1 + r^2\iota^2/(2\pi R)^2]}, \qquad \frac{r}{R} \ll 1. \end{aligned} \tag{30}$$

Insertion of this into Eq. (3) determines the rate of decay of density on a magnetic surface,

$$\frac{\partial \rho}{\partial t} = \frac{1}{r}\frac{\partial}{\partial r} r \frac{2\eta c^2 kT}{mB^2}\left[1 + \frac{8\pi^2}{\iota^2}\right]\rho \frac{\partial \rho}{\partial r}. \tag{31}$$

A similarity solution [23] can be found by assuming that $\rho = \rho_0 X(r)\, W(t)$. Then

$$\rho = \rho_0 X(r)/[1 + (2\eta c^2 kT/m)\, \lambda t], \tag{32}$$

with $X(r)$ and λ determined from

$$\frac{1}{r}\frac{d}{dr}\frac{r(1 + 8\pi^2/\iota^2)\,\rho_0}{B^2}\frac{dX}{dr} = -\lambda X. \tag{33}$$

The characteristic value λ is fixed by the boundary conditions $X = 1$ and $dX/dr = 0$ at $r = 0$, and $X = 0$ at the boundary. For a straight system $J_\parallel$ can be zero and the Pfirsch–Schlüter factor $(1 + 8\pi^2/\iota^2)$ can be set equal to one.

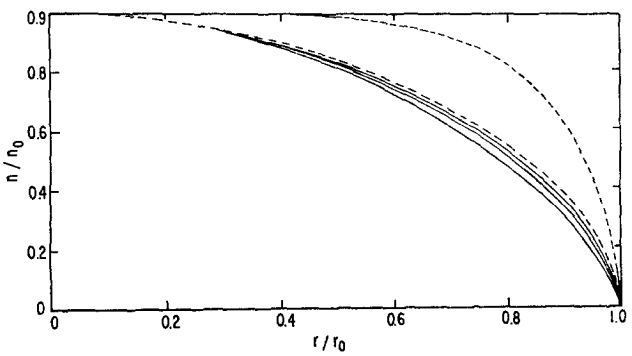

FIG. 3. Similarity solutions for diffusion in a torus. The lower dashed curve denotes the average radial density distribution due to the classical Pfirsch–Schlüter flux in a magnetic geometry with a uniform rotational transform (an $l = 2$ stellarator). The solid curves are the results of numerical simulation for one, two, and three times the classical value of resistivity. Enhancing the resistivity increases surface flow velocities and radial flux, causing the profile to lie lower. The upper dashed curve represents the classical distribution for a parabolic transform (an $l = 3$ stellarator). The results of numerical simulation for the same resistivities are indistinguishable from the classical result on this scale.

The lower dotted curve in Fig. 3 shows the solution $X(r)$ for a straight configuration with $n_0 = 10^{13}$ cm^{-3} hydrogen at 100 eV, $B_z = 10^4$ G, and $f = B_\theta/B_z = 0.1(r/a)$. This choice of f corresponds to a uniform rotational transform (an $\ell = 2$ stellarator). The curve for a parabolic rotational transform [$f = 0.1(r/a)^3$, corresponding to an $\ell = 3$ stellarator] is the same. The effect of curvature on the solution of

Eq. (31) is not particularly striking if the rotational transform is constant. For an aspect ratio R/a of 10, the curve again lies on the cylinder curve. The Pfirsch–Schlüter factor introduces a significant modification for an $\ell = 3$ stellarator: As shown by the other dotted curve, the pressure gradient must vanish in the region where the transform is small.

To see the effects of inertia we numerically adjusted the distributions to obtain self-consistent similarity solutions with zero average flow on a surface.

In the absence of toroidal curvature we were able to use extremely large values of resistivity to speed the calculation, and found that with any static initial density distribution the system quickly adjusted to that satisfying Eq. (33) and then proceeded to decay in agreement with Eq. (32).

In toroidal systems we found it necessary to modify the model to "short-circuit" the radial electric field, thus inhibiting rotation. The resulting radial profiles of average density are presented in Fig. 3. As previously mentioned, the dotted curves represent the average density on the magnetic surfaces for systems with a constant rotational transform and with a parabolic transform, for the case of very small resistivity. The solid lines correspond to one, two, and three times the classical resistivity [24]. For these cases the plasma loss is enchanced over that predicted by quasistatic theory because the density is no longer constant on a magnetic surface; it is higher on the outside of the torus and lower on the inside. The electrostatic field associated with $\eta J_{\|}$ tends to move the plasma toward the outside, so the loss is increased.

The diffusion rate, defined as the mass flow through a magnetic surface divided

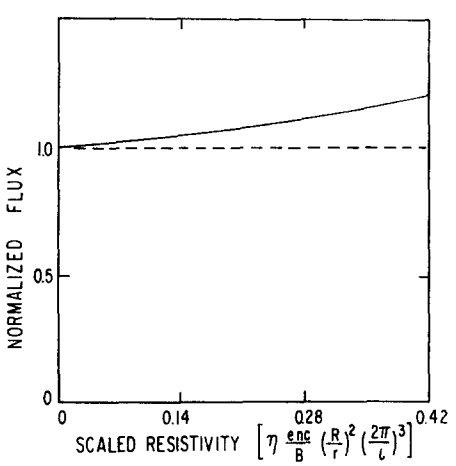

FIG. 4. Mass flux for similarity solutions. The indicated values of η correspond to zero, one, two, and three times the classical resistivity.

by the mass inside this surface, is a constant (independent of radius) for a similarity solution. This quantity, divided by its quasistatic value, is plotted as a function of resistivity in Fig. 4. The departure from the quasistatic value is due to the increase in pressure on the outside of the torus, which balances the inertial acceleration associated with surface flow.

5. Plasma Rotation

Recent studies [8, 9, 17, 18], based on a variety of models, have indicated that a plasma confined in a toroidal configuration tends to rotate. These analyses demonstrate that in the presence of resistivity a static configuration is not stable. Although some work [9] has shown that viscosity is important in the determination of a steady-state configuration, it is obviously of interest to study this behavior on the simplest possible model. Therefore, we used our numerical simulation model to follow the long-time behavior of an initially static configuration.

In a typical calculation we assumed that $T_e = T_i = 25$ eV, $B = 10^4$ G, $R = 100$ cm, $a = 5$ cm, $\eta = \eta_{\text{Spitzer}}$ [25], and we use a smooth density profile in the starting conditions.

In Fig. 5 we display the time evolution of the rotation velocity v_θ normalized

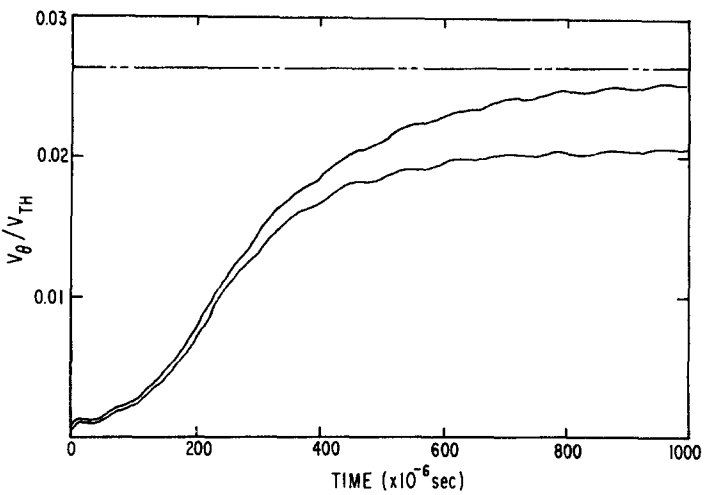

FIG. 5. Development of plasma rotation. The lower curve denotes the average poloidal rotation velocity, divided by the ion sound speed, as a function of time. The upper curve represents v_θ/v_{th} at the inside ($\theta = 0$) of the torus. The broken line is the projection of the thermal velocity along **B** upon the poloidal basis vector. The starting conditions correspond to a nearly static equilibrium.

to the thermal velocity. The two curves correspond to the velocity averaged over the magnetic surface, and to the velocity at $\theta = 0$ (on the inside of the torus). Results are presented for a surface at 4 cm radius, where the initial density gradient is a maximum. Behavior on the neighboring surfaces is similar. At late times the net outward flow is roughly 1.3 times that predicted by the Pfirsch–Schlüter formula.

The major features of these curves are the exponential growth of the rotation velocity and the saturation at a value somewhat below the dotted line corresponding to $v_\theta = fv_{\text{th}} = (B_\theta/B_z)\, v_{\text{th}}$. Superimposed on this is an acoustic wave with a period identified with the geodesic mode. This oscillation can be reduced or eliminated by carefully choosing the initial conditions. We do this to avoid

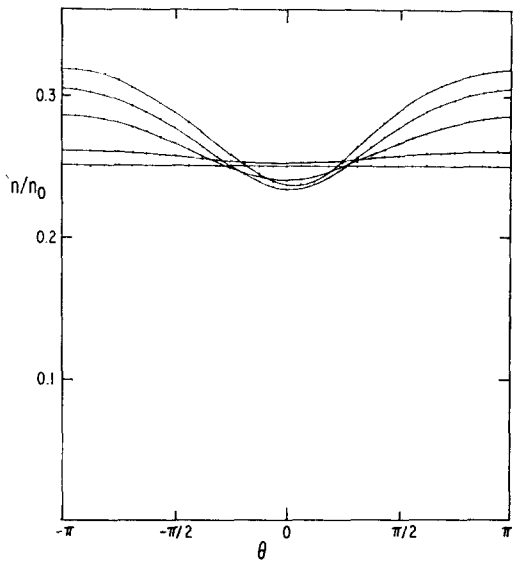

FIG. 6. Surface density variations with rotation. The curves represent the variation of mass density with azimuth at 0, 250, 500, 750, and 1000 microseconds into the calculation of Fig. 5. At $\theta = \pi$, the density monotonically increases with time due to resistive diffusion. The dots correspond to the mesh points in the finite-difference grid.

overwhelming the slower diffusion and rotation processes with large-amplitude acoustic oscillations. The numerical and physical damping of these modes is very small, so that "transient modes" excited by the initial conditions have a damping time which is long compared to the development time of the features of physical interest.

Viewed as a density perturbation, the initial transient is very small, roughly

10^{-3} times the average density. Figure 6 presents the time development of the density distribution on this magnetic surface. It shows a pronounced outward shift (toward $\theta = \pi$) of the density. Superimposed on this shift is an increase with time of the total mass on the surface, due to resistive diffusion into it.

On the basis of analytic studies utilizing the ideal model with a large aspect ratio expansion, the character of fluid flow should change when the average rotation reaches $v_\theta = fv_{\text{th}}$; we should expect v_θ to approach this value. Since collisional viscosity should modify this singular behavior, which is displayed by the analysis [11], we first thought that the numerical viscosity associated with the grid was responsible for the magnitude of this difference, $fv_{\text{th}} - v_\theta$. Work with finer meshes suggested that this is not the case.

The plasma flow on a magnetic surface is closely analogous to the problem of flow through a nozzle [26], the $(1 - r\cos\theta/R)$ metric coefficient playing a role similar to the cross-sectional area in the classical hydrodynamic problem. Thus we should expect a sonic point to occur at $\theta = 0$. Hazeltine, Lee, and Rosenbluth [17] have carried through an analysis verifying this. The curve for $v_\theta(\theta = 0)$ agrees with such a model.

Clearly, further work in this direction would be useful. An asymptotic analysis of this behavior, using the inverse aspect ratio as an expansion parameter, has been performed and will be reported shortly [18]. An analysis of diffusion in these steady-state systems with flow, similar to the one reported in Section 3 for static systems, should be developed.

For our model, the time evolution of v_θ has mirror symmetry about $v_\theta = 0$; the plasma can spin in either direction, saturating *at* $|v_\theta| \simeq fv_{\text{th}}$. However, recent calculations [27] which include the inhibition of plasma and current flow parallel to **B** caused by viscosity in the presence of magnetic field corrugations, remove the degeneracy in the direction of rotation. We find that the plasma becomes positively charged in the center, and takes on the corresponding $\mathbf{E} \times \mathbf{B}$ rotation.

Appendix I

Here we examine the numerical stability of the finite differencing scheme for small-amplitude perturbations. We follow the method of Richtmyer and Morton [21]; for simplicity we neglect the effect of resistivity. We treat two limiting cases; in each case one mode of oscillation is dominant.

First we consider the case of small rotational transform. Then the parallel acoustic period is long and the geodesic mode dominates. Small perturbations $\tilde{\rho}$, $\tilde{v}$ satisfy the continuity equation,

$$\frac{\partial \tilde{\rho}}{\partial t} = -\rho_0 \nabla \cdot \tilde{\mathbf{v}}, \tag{I.1}$$

and

$$\int \left[2kT\,\nabla\tilde{\rho} + m\rho_0 \frac{\partial \tilde{\mathbf{v}}}{\partial t}\right] \cdot \mathbf{e}_s N^2\, d\theta = 0, \tag{I.2}$$

which results from substituting Eq. (1) into Eq. (13). If we express the radial velocity in terms of the average potential, then to lowest order in r/R the difference form of these equations is

$$\tilde{\rho}_\theta^{t+1} - \tilde{\rho}_\theta{}^t = -\frac{\delta t}{R}\,\rho_0(\bar{\phi}')^{t+1/2} \sin\theta \tag{I.3}$$

and

$$(\bar{\phi}')^{t+1/2} - (\bar{\phi}')^{t-1/2} = \frac{4kT}{m\rho_0 r}\,\frac{\delta t}{N_\theta} \sum_{\theta=1}^{N_\theta} \tilde{\rho}_\theta{}^t \sin\theta. \tag{I.4}$$

Clearly this couples the average potential to the $\sin\theta$ component of $\tilde{\rho}$. If we assume a harmonic time dependence $e^{-i\omega t}$, the frequency of a perturbation is given by

$$\cos\omega\,\delta t = 1 - \frac{kT}{mR^2}(\delta t)^2, \tag{I.5}$$

and ω is real provided

$$\delta t < R(2m/kT)^{1/2}. \tag{I.6}$$

Now consider the case of very small curvature. The geodesic period becomes long, and the parallel mode dominates. It is characterized by the continuity equation and the parallel component of the force equation. Their difference formulations are

$$\begin{aligned}\tilde{\rho}_\theta^{t+1} - \tilde{\rho}_\theta{}^t = &-\frac{\delta t}{\delta\theta}\frac{f}{r}(1+f^2)^{-1/2}\,\rho_0[(\tilde{v}_\parallel)_{\theta+1/2}^{t+1/2} - (\tilde{v}_\parallel)_{\theta-1/2}^{t+1/2}] \\ &- \frac{u}{2}(1+f^2)^{-1/2}\,[\tilde{\rho}_{\theta+1}^{t+1/2} - \tilde{\rho}_{\theta-1}^{t+1/2}]\end{aligned} \tag{I.7}$$

and

$$\begin{aligned}(\tilde{v}_\parallel)_{\theta+1/2}^{t+1/2} - (\tilde{v}_\parallel)_{\theta+1/2}^{t-1/2} + u[(\tilde{v}_\parallel)_{\theta+1/2}^{t-1/2} - (\tilde{v}_\parallel)_{\theta-1/2}^{t-1/2}] \\ = -\frac{2fkT}{m\rho_0 r}\,\frac{\delta t}{\delta\theta}(1+f^2)^{-1/2}\,[\tilde{\rho}_{\theta+1}^{t} - \tilde{\rho}_\theta{}^t].\end{aligned} \tag{I.8}$$

Here $u = v_\theta\,\delta t/r\,\delta\theta \geqslant 0$. If u were less than zero, the space difference on $\tilde{v}_\parallel$ would be between $\theta + 3/2$ and $\theta + 1/2$. We write Eq. (I.7) at two successive time steps

and subtract, and then eliminate $\tilde{v}_{\parallel}$ through Eq. (I.8). Assuming a dependence of the form $\tilde{\rho}(\theta, t) = T^t \Theta^\theta$, and writing $\eta = T^{\delta t}$ and $\xi = \Theta^{\delta\theta}$, we obtain

$$\eta^3 - \left[2 - \alpha^2(2 - \xi - \xi^{-1}) - \frac{u}{4}(3\xi + 4 - \xi^{-1})\right]\eta^2 + [1 - u(1 + \xi)]\,\eta + \frac{u}{4}(\xi + \xi^{-1}) = 0, \tag{I.9}$$

where

$$\alpha = \frac{\delta t}{\delta\theta}\frac{f v_{\text{th}}}{r(1 + f^2)^{1/2}}.$$

This is of third order in η because of the backward difference required to compute $\tilde{\rho}$ at the half-time. For $\alpha^2 \ll 1$ and $u \ll 1$, one root of Eq. (I.9) is small, $\eta \simeq u(\xi + \xi^{-1})/4$. This root can be factored out of Eq. (I.9), and the other two roots, to first order in α^2 and u, are

$$\eta = 1 - w \pm [w^2 - \alpha^2(2 - \xi - \xi^{-1})]^{1/2}, \tag{I.10}$$

where

$$w = \frac{\alpha^2}{2}(2 - \xi - \xi^{-1}) + \frac{u}{4}(2 + \xi - \xi^{-1}).$$

The root that is larger in magnitude satisfies $|\eta|^2 = 1 - u(2 + \xi + \xi^{-1})/2$ to lowest order in w, so $|\eta| < 1$ unless $u = 0$. Thus the numerical scheme is stable, provided $\alpha^2 \ll 1$, $u \ll 1$. Numerical studies of the cubic equation for finite values of α and u indicate that the scheme is stable for $\alpha < 1/4$, $u < 0.75$. In terms of the physical parameters, this limits the time step to

$$\delta t < \tfrac{1}{4}[1 + 4\pi^2(R^2 - r^2)/r^2 t^2]^{1/2}\, r\,\delta\theta/v_{\text{th}} \tag{I.11}$$

or

$$\delta t < \tfrac{3}{4} r\,\delta\theta/v_\theta, \tag{I.12}$$

whichever is smaller.

The finite difference scheme reduces to either Eqs. (I.3) and (I.4) or Eqs. (I.7) and (I.8), in the two respective limits. We therefore choose our time step to satisfy the most restrictive criterion of Eqs. (I.6), (I.11), or (I.12). For the parameters discussed in Section 5, the most restrictive is Eq. (I.11) evaluated on the surface nearest the magnetic axis. It limits δt to a few microseconds. The calculations reported in that section were performed with a time step of 1 μ sec.

In the calculations of this paper, the time step has been adjusted to satisfy Eq. (I.11) on the inner surface. Since the density gradients are small the flow

remains slow in this region and has little effect on the overall behavior of the plasma. The small time step insures that the numerical calculations are accurate in the outer region. In particular, the $\partial \mathbf{v}_\perp/\partial t$ term in Eq. (1) is replaced by its value from the previous time step, as discussed above Eq. (10). This introduces an error, of order $\rho\omega_\perp\, \delta t$ times the root-mean-square time average of $\partial \mathbf{v}_\perp/\partial t$, into the left side of Eq. (1). (Here $\omega_\perp$, the geodesic acoustic frequency, corresponds to the shortest characteristic time in the model.) For our parameters this error is a factor of 10^2 smaller than the truncation error in the centered-difference approximation to ∇p. For the parameters used in Section 5, but modified to approximate the first limiting case of this appendix, the geodesic mode amplitude is constant to within five parts in 10^5 per period (one part in 10^3 for the duration of the calculation in Fig. 5). For similar parameters, the lowest parallel acoustic mode decays by five parts in 10^4 per period (one part in 10^2 for the calculation of Fig. 5).

The preceding analysis describes the linear behavior of the model. For a more complete understanding of the model, it is necessary to examine its nonlinear behavior. This was obtained from many numerical experiments with the normal modes excited by the initial conditions (both intentionally and unintentionally). When flow and diffusion are important, the results are in qualitative agreement with what one expects from mode coupling and resistive diffusion.

Appendix II

Equation (13) can be converted into a partial differential equation that advances the average potential in time by writing $\mathbf{v}$ in such a way as to explicitly exhibit its dependence on $\bar{\phi}$. Thus

$$\mathbf{v} = c\,\frac{\mathbf{B}}{B^2} \times \bar{\phi}'\,\nabla\Psi + \tilde{\mathbf{v}}, \tag{II.1}$$

where $\bar{\phi}' = \partial\bar{\phi}(\Psi)/\partial\Psi$. Straightforward vector manipulation converts Eq. (13) to the form

$$\oint \frac{dS}{B}\Bigg\{\rho c\left[\frac{\nabla\Psi}{B}\left(\frac{\partial\bar{\phi}'}{\partial t} + \bar{\phi}''\tilde{\mathbf{v}}\cdot\nabla\Psi\right) + \bar{\phi}'\tilde{\mathbf{v}}\cdot\nabla\frac{|\nabla\Psi|}{B}\right]$$
$$+ \frac{\mathbf{B}\times\nabla\Psi}{B|\nabla\Psi|}\cdot\left[\frac{2kT}{m}\nabla\rho + \frac{1}{2}\rho\nabla\left|\frac{c\nabla\Psi}{B}\bar{\phi}'\right|^2 + \rho\left(\frac{\partial\tilde{\mathbf{v}}}{\partial t} + \tilde{\mathbf{v}}\cdot\nabla\tilde{\mathbf{v}}\right)\right.$$
$$\left.+ \rho c\frac{|\nabla\Psi|}{B}\bar{\phi}'\frac{\mathbf{B}\times\nabla\Psi}{B|\nabla\Psi|}\cdot\nabla\tilde{\mathbf{v}}\right]\Bigg\} = 0. \tag{II.2}$$

Since $\bar{\phi}'$ depends only on Ψ it can be removed from the surface integrals, so that

$$\frac{\partial \bar{\phi}'}{\partial t} + \beta \frac{\partial \bar{\phi}'}{\partial \Psi} + \gamma(\bar{\phi}')^2 + \delta\bar{\phi}' + \epsilon = 0, \tag{II.3}$$

with

$$\beta \equiv \oint \frac{dS}{B^2} \rho \mid \nabla\Psi \mid \tilde{\mathbf{v}} \cdot \nabla\Psi \Big/ \oint \frac{dS}{B^2} \rho \mid \nabla\Psi \mid,$$

$$\gamma \equiv \frac{c}{2} \oint \frac{dS}{B} \rho \mathbf{e}_s \cdot \nabla \left| \frac{\nabla\Psi}{B} \right|^2 \Big/ \oint \frac{dS}{B^2} \rho \mid \nabla\Psi \mid,$$

$$\delta \equiv \oint \frac{dS}{B} \rho \left\{ \tilde{\mathbf{v}} \cdot \nabla \frac{\mid \nabla\Psi \mid}{B} + \frac{\mid \nabla\Psi \mid}{B} \mathbf{e}_s \cdot (\nabla\tilde{\mathbf{v}}) \cdot \mathbf{e}_s \right\} \Big/ \oint \frac{dS}{B^2} \rho \mid \nabla\Psi \mid,$$

and

$$\epsilon \equiv \frac{1}{c} \oint \frac{dS}{B} \mathbf{e}_s \cdot \left[\frac{2kT}{m} \nabla\rho + \rho \left(\frac{\partial \tilde{\mathbf{v}}}{\partial t} + \tilde{\mathbf{v}} \cdot \nabla\tilde{\mathbf{v}} \right) \right] \Big/ \oint \frac{dS}{B^2} \rho \mid \nabla\Psi \mid.$$

Here $\mathbf{e}_s = \mathbf{B} \times \nabla\Psi / B \mid \nabla\Psi \mid$ is a unit vector tangent to the magnetic surface, perpendicular to $\mathbf{B}$.

ACKNOWLEDGMENTS

We are indebted to Dr. J. M. Greene for many helpful discussions and suggestions during the course of this work and for carefully reading and criticizing the manuscript. Dr. J. Hogan informed us of Longmire's analysis of similarity solutions for the diffusion discussion.

REFERENCES

1. M. D. KRUSKAL AND R. M. KULSRUD, *Phys. Fluids* **1** (1958), 265.
2. V. D. SHAFRANOV, *in* "Reviews of Plasma Physics" (M. A. LEONTOVICH, Ed.), Vol. 2, p. 103, Consultants Bureau, New York, 1966.
3. J. M. GREENE AND J. L. JOHNSON, *Phys. Fluids* **4** (1961), 875.
4. J. M. GREENE AND J. L. JOHNSON, *in* "Advances in Theoretical Physics" (K. BRUECKNER, Ed.), Vol. 1, p. 195, Academic Press, New York, 1965.
5. G. KNORR, *Phys. Fluids* **8** (1965), 1334.
6. E. T. KARLSON, *Ark. Fys.* **35** (1968), 539.
7. K. S. VISWANATHAN, *Phys. Fluids* **11** (1968), 1104.
8. T. E. STRINGER, *Phys. Rev. Lett.* **22** (1969), 770.
9. M. N. ROSENBLUTH AND J. B. TAYLOR, *Phys. Rev. Lett.* **23** (1969), 367.
10. A. S. BISHOP AND C. G. SMITH, *Phys. Fluids* **9** (1966), 1380.
11. A. GIBSON AND J. B. TAYLOR, *Phys. Fluids* **10** (1967), 2653.

12. C. G. SMITH AND A. S. BISHOP, *in* "Plasma Physics and Controlled Nuclear Fusion Research," Vol. I, p. 591, International Atomic Energy Agency, Vienna, 1969.
13. H. GRAD AND J. HOGAN, *Bull. Amer. Phys. Soc.* **14** (1969), 1017.
14. D. PFIRSCH AND A. SCHLÜTER, Max Planck Institute Report MPI/PA/7/62 (1962), unpublished.
15. N. K. WINSOR, J. L. JOHNSON, AND J. M. DAWSON, *Phys. Fluids* **11** (1968), 2448.
16. J. L. JOHNSON AND S. VON GOELER, *Phys. Fluids* **12** (1969), 255.
17. R. D. HAZELTINE, E. P. LEE, AND M. N. ROSENBLUTH, to be published.
18. J. M. GREENE, J. L. JOHNSON, K. E. WEIMER, AND N. K. WINSOR, to be published.
19. L. SPITZER, JR., "Physics of Fully Ionized Plasmas," 2nd edition, p. 27 et seq., John Wiley and Sons, New York, 1962.
20. K. V. ROBERTS, *in* "Symposium on Computer Simulation of Plasma and Many-Body Problems," p. 163, National Aeronautics and Space Administration, Washington, D. C., NASA SP-153, 1967.
21. R. D. RICHTMYER AND K. W. MORTON, "Difference Methods for Initial-Value Problems," Chapter 10, John Wiley and Sons, New York, 1967.
22. Reference [21], Chapter 12.
23. C. L. LONGMIRE, "Elementary Plasma Physics," p. 228 et seq., John Wiley and Sons, New York, 1963.
24. Reference [19], p. 43.
25. Reference [19], p. 139.
26. J. M. GREENE, private communication.
27. N. K. WINSOR, J. L. JOHNSON, AND J. M. DAWSON, *Bull. Amer. Phys. Soc.* **14** (1969), 1037; N. K. WINSOR, to be published.